

Microtubule instability driven by longitudinal and lateral strain propagation

Maxim Igaev^{1,*}, Helmut Grubmüller^{1,*}

¹ Max Planck Institute for Biophysical Chemistry, Am Fassberg 11, D-37077 Göttingen, Germany

* E-mail: migaev@mpibpc.mpg.de or hgrubmu@gwdg.de

Abstract

1 Tubulin dimers associate longitudinally and laterally to form metastable microtubules (MTs). MT
2 disassembly is preceded by subtle structural changes in tubulin fueled by GTP hydrolysis. These
3 changes render the MT lattice unstable, but it is unclear how exactly they affect lattice energetics
4 and strain. We performed long-time atomistic simulations to interrogate the impacts of GTP
5 hydrolysis on tubulin lattice conformation, lateral inter-dimer interactions, and (non-)local lateral
6 coordination of dimer motions. The simulations suggest that most of the hydrolysis energy is
7 stored in the lattice in the form of longitudinal strain. While not significantly affecting lateral bond
8 stability, the stored elastic energy results in more strongly confined and correlated dynamics of
9 GDP-tubulins, thereby entropically destabilizing the MT lattice.

Introduction

11 Microtubules (MTs) are one of the major components of the eukaryotic cytoskeleton and essential
12 for intracellular transport, cell motility, and chromosome separation during mitosis. These are
13 filamentous assemblies of $\alpha\beta$ -tubulin dimers stacked head-to-tail in polar protofilaments (PFs)
14 and folded into hollow tubes via lateral interactions [1,2] (Fig. 1a). Each dimer binds two GTP
15 molecules of which only the one bound to β -tubulin is hydrolyzed in the MT lattice over time [3,4].
16 This hydrolysis reaction is fundamental to MT dynamic instability [5], *i.e.* random switching
17 between phases of growth and shrinkage (Fig. 1a). Remarkably, both slow assembly and rapid
18 disassembly of MTs – the latter termed *catastrophe* – are able to perform mechanical work because
19 each tubulin dimer is a storage of chemical energy [6–8].

20 The switch from a relaxed ‘curved’ conformation of tubulin favored in solution to a higher-energy
21 ‘straight’ one is inherent to MT assembly [9–15]. It allows growing MTs to recruit and temporarily
22 stabilize GTP-tubulin in the straight form, most likely due to the greater bending flexibility of GTP-
23 PFs at intra- and inter-dimer interfaces [13,16–18]. It is therefore conceivable that collapsing MTs
24 would follow a reverse pathway during disassembly; namely, they would release the conformational
25 tension stored in GDP-tubulins that lateral bonds can no longer counteract. However, due to
26 the system complexity and together with the inability of modern structural methods to directly
27 visualize all sequential steps in the GTPase cycle in the straight MT body at high resolutions, it is
28 still unknown exactly how and where the hydrolysis energy is converted to mechanical strain in the
29 lattice.

30 Recent high-resolution cryo-EM studies have revealed, in line with the early finding [19], that
31 GTP hydrolysis triggers changes in α -tubulin, resulting in a subnanometer longitudinal lattice
32 compaction (Fig. 1b) [20–23]. Because by itself this global lattice rearrangement does not fully
33 indicate how it is linked to the strain accumulation at the single-dimer level, two competing scenarios
34 have been proposed [24]. According to the *seam-centric* or *strain* model of MT catastrophe [20–22],

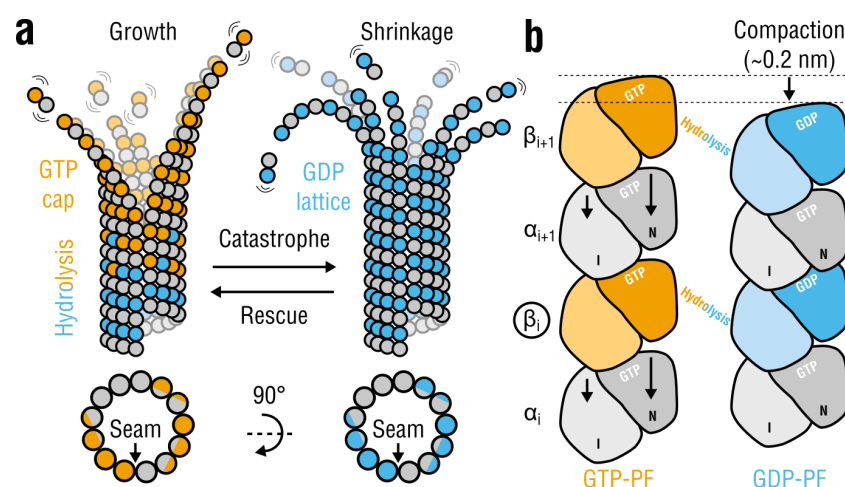


Figure 1. Tubulin life cycle and lattice compaction upon GTP hydrolysis. **a**, Cartoon representation of structural intermediates in MT assembly and disassembly. Individual dimers are composed of α -tubulins (gray circles) and β -tubulins (orange circles when GTP-bound or cyan circles when GDP-bound). Lattice cross-sections (bottom) indicate the location of the seam interface. **b**, Local conformational changes proposed to accompany GTP hydrolysis are shown schematically (viewed from within the lumen). Each monomer is illustrated as two domains: intermediate or I and nucleotide-binding or N (C-terminal domains are not shown). Rearrangements in α -tubulin around the nucleotide-binding pocket at the inter-dimer interface result in a ~ 0.2 -nm lattice compaction. The PFs are aligned with respect to monomer β_i (marked with a circle). Other more subtle changes (*e.g.*, PF twisting) or intermediate nucleotide states (*e.g.*, GDP-Pi) are not shown for simplicity.

the gradual build-up of longitudinal tension along the lattice upon GTP hydrolysis is the primary source of MT instability, where the lateral interfaces play only a passive role. In this model, lattice rupture is initiated at the seam because of the greater distance, and presumably weaker interactions, between PFs at this interface observed in unsymmetrized cryo-EM reconstructions. In contrast, the *holistic* or *bond* model [23,24] assumes that MT catastrophe can be explained by a sequential weakening of lateral inter-dimer contacts accompanied by a simultaneous strengthening of longitudinal contacts. Here, the exceptional mechanical weakness of the seam, which has been challenged recently [25], is not a prerequisite for MT catastrophe.

The coexistence of the two models originates from the fact that the interplay between tubulin intrinsic strain and lateral binding inside the straight MT body is largely unclear. Indeed, the subtle changes in lattice compaction and dimer-dimer contacts would be best studied within straight PF assemblies in the presence or absence of lateral neighbors and conditioned on a fixed nucleotide state, which has not yet been achieved. This has prompted us to assess the mechanochemistry of both lattice compaction and lateral inter-dimer coupling using extensive molecular dynamics (MD) simulations of (i) isolated PFs, (ii) standard (homotypic) double-PF systems, as well as (iii) three-PF lattice patches. In all cases the PFs were locked in the straight conformation due to the use of periodic boundaries along the MT axis, thereby mimicking lattice regions distant from the dynamic tip. By focusing on small, controllable MT-like subsystems, our simulations provide new insights into the lattice mechanics and energetics that drive MT disassembly.

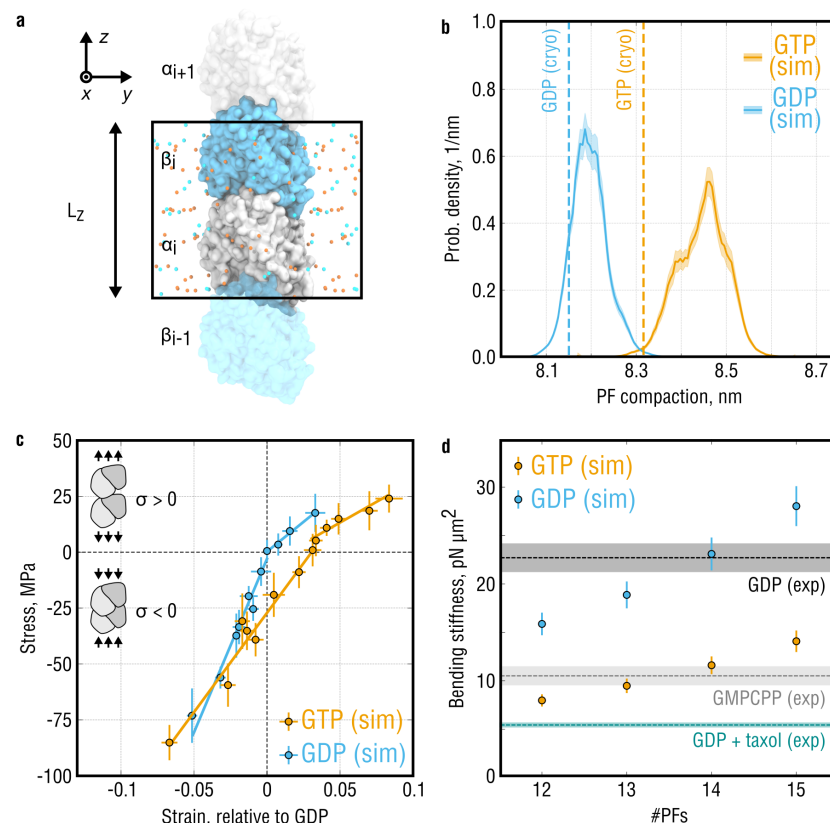


Figure 2. Elastic properties of isolated 'infinite' PFs. **a**, Simulation setup for the single-PF system. α -tubulin (gray) and β -tubulin (cyan) are shown in surface representation. Potassium and chloride ions are shown as orange and cyan spheres, respectively. Water molecules are hidden for clarity. Periodic box with the axial dimension L_z (dimer rise) is marked by a black rectangle. **b**, Equilibrium probability distributions of PF compaction (expressed in units of L_z) obtained from stress-free simulations of the system in **a**. Shaded areas show statistical uncertainties of the distributions estimated with umbrella sampling. Dashed lines indicate PF compaction values observed in the cryo-EM densities of GMPCPP- and GDP-MTs. **c**, Stress-strain curves calculated for the system in **a** in both GTP- (orange) and GDP-state (cyan). Strain is computed relative to the equilibrium dimer length of GDP-PF, and negative (positive) stresses correspond to PF compression (extension). **d**, Bending stiffness parameters of GTP- and GDP-MTs calculated using the elastic moduli in **b** (negative stresses) and for varying PF numbers (orange and cyan dots, respectively). Experimental values (dashed lines with shaded areas) represent inverse-variance weighted means and standard deviations that combine multiple independent thermal fluctuation measurements summarized in [26] and recently updated in [27].

Results

GTP hydrolysis in β -tubulin stiffens individual PFs

If MTs accumulate longitudinal elastic strain upon GTP hydrolysis, one would expect them to change the mechanical properties of individuals PFs also in the absence of lateral interactions. We therefore asked how the nucleotide state affects both equilibrium conformation and elasticity of isolated PFs and how much mechanical energy can be potentially stored in a single dimer upon GTP hydrolysis. The recent cryo-EM reconstructions of MTs in non-hydrolyzable GMPCPP-

(here referred to as GTP for simplicity) and GDP-state [21,22] enabled us to construct atomistic models of isolated PFs (Fig. 2a) using correlation-driven molecular dynamics [28] and to assess their equilibrium and elastic properties by atomistic MD simulations (see Methods for details on system preparation, cryo-EM model refinement, simulation protocol).

To assess the equilibrium properties of isolated PFs at room temperature, we first performed multiple simulations of GTP- and GDP-PFs totaling $\sim 23 \mu\text{s}$ and $\sim 13 \mu\text{s}$, respectively, following a previously published protocol [29]. We monitored the dynamics of tubulin dimer shape and spacing in the PFs, the latter expressed in terms of the axial periodic parameter L_z (Fig. 2a), which was a measure of PF compaction. Figure 2b shows the equilibrium probability distributions of PF compaction as a function of the nucleotide state computed with additional umbrella sampling simulations, where we used L_z as a reaction coordinate ($\sim 114 \mu\text{s}$ of cumulative simulation time; see Methods). Both GTP- and GDP-PFs slightly increased the lattice period during the simulations relative to their initial cryo-EM conformations due to thermal expansion. However, GTP-PFs maintained a significantly longer monomer repeat compared with GDP-PFs ($+0.25 \pm 0.07 \text{ nm}$), consistent with the experimentally observed difference of $\sim 0.2 \text{ nm}$. In the following, we will refer to these two states as *expanded* and *compacted*. Hence, it is likely that the difference between the global states of MT structure seen by cryo-EM reflects a local response of tubulin to GTP hydrolysis; otherwise, it would vanish in the absence of lateral contacts.

Further, GTP-PFs sampled a wider range of PF compaction values as indicated by the distribution widths in Fig. 2b, which suggests that GTP-PFs are mechanically more flexible. We previously showed that, when placed in solution, GTP-tubulin exhibits higher bending flexibility than GDP-tubulin [17]. It was therefore surprising that, when tubulin was locked in the straight MT-like conformation, also the longitudinal elasticity of the dimer was affected by the nucleotide state.

To quantify the mechanical elasticity of the system in Fig. 2a, we performed a set of steady-state compression/extension simulations at constant values of the axial component P_{zz} of the pressure tensor (along the PF). Figure 2c shows the obtained strain-stress curves, where the strain was computed relative to the equilibrium conformation of GDP-PFs. Irrespective of the nucleotide state, the stress-strain data clearly falls into two elastic regimes: a rather soft response for positive stresses (extension) and a much stiffer response for negative stresses (compression). This previously observed behavior of GDP-tubulin [29], which we here confirmed using higher quality structures of both nucleotide states and wider strain ranges, emerges likely because different parts of the heterodimer are involved in the mechanical response upon compression or extension. Whereas extension mainly stretches the inter-dimer and, to a lesser extent, intra-dimer interfaces, compression forces individual monomers to change their shapes, causing much more resistance. We therefore analyzed the positive and negative strain ranges separately.

A linear fit to the negative stress data of the GTP- and GDP-PF simulations yielded elastic moduli of $0.89 \pm 0.07 \text{ GPa}$ and $1.77 \pm 0.13 \text{ GPa}$, respectively. Fitting to the positive stress data yielded systematically smaller moduli of $0.37 \pm 0.07 \text{ GPa}$ (GTP-PF) and $0.53 \pm 0.03 \text{ GPa}$ (GDP-PF). Whereas the single-PF system tolerated high compression stresses up to $P_{zz} = +200 \text{ bar}$ without undergoing plastic deformations and irrespective of the nucleotide state, this was not the case for extension stresses. GTP-PFs withstood stretching up to $P_{zz} = -65 \text{ bar}$ without rupturing at the inter-dimer interface in the course of our simulations ($\sim 1 \mu\text{s}$ each). In contrast, GDP-PFs ruptured already at stress values below $P_{zz} = -40 \text{ bar}$, implying that a lower force is likely sufficient to break the longitudinal bond. Although more sampling would be required to investigate PF rupture pathways, our stress-strain data (Fig. 2c) together with the equilibrium free energy calculations (Fig. 2b) support the interpretation that straight GDP-PFs are stiffer than GTP-PFs while they might possess more fragile inter-dimer longitudinal bonds.

The factor of two difference in the elastic moduli of GTP- and GDP-PFs is remarkable given the high initial similarity of the two conformational states. Careful review of existing measurements of MT bending mechanics reveals that, despite variations in the experimental protocols and theoretical models used to analyze such data, MTs are intrinsically softer when polymerized in the presence of

GMPCPP and/or Taxol [26,27]. This is reflected, *e.g.*, in a significantly distinct bending stiffness $E \times I$, where E is the elastic modulus and I is the second moment of the cross-sectional area of the MT. We therefore asked if the nucleotide-dependent elasticity of PFs (Fig. 2*b,c*) might explain the experimentally observed differences in coarse-grained elastic properties of MTs.

Bending stiffness of MTs is typically obtained either by quantifying their equilibrium thermal fluctuations that probe small-strain deformations or by applying external forces that induce high-strain deformations [26]. We hence compared our calculations only with thermal fluctuation experiments because non-elastic deformations as well as induced contact breaking are less likely to occur under such conditions, consistent with our small-strain simulations. Figure 2*d* compares bending stiffnesses of hypothetical MTs with varying PF numbers calculated using our data in Fig. 2*c* (negative stresses) and consensus values calculated as precision-weighted averages from a pool of independent experimental measurements (reviewed in [26] and recently updated in [27]; see Methods). The comparison revealed that a good agreement between the experimental data and our calculations can only be achieved if the PF number is strictly 14 for GDP-MTs and 13-14 for GTP-MTs. It is known that MT mechanics is highly sensitive to changes in the PF number (see Discussion in [30]). Most MTs polymerized *in vitro* without co-factors and MT-binding drugs possess 14 PFs [31], with ratios of 13-PF to 14-PF MTs reaching approximately 1:9 for GDP-MTs and 1:3 for GMPCPP-MTs [21,22]. Assuming that tubulin axial elasticity does not depend on the PF number, the two-fold higher bending stiffness of GDP-MTs can be accounted for almost entirely by a two-fold higher elastic modulus of GDP-PFs, at least for small-strain deformations.

Finally, the good agreement of our elasticity calculations with experimental knowledge allowed us to estimate that a free energy of $\Delta G_{\text{el}} \approx 11.6 \text{ k}_B\text{T}$, where k_B is the Boltzmann constant, would be stored in a GTP-PF per dimer when mechanically compressed to the state of a GDP-PF (see Supplementary Material). Remarkably, this energy is very close to both the energy harvested by MTs upon GTP hydrolysis [19,32] and the maximal excess energy that can be stored in a MT lattice to maintain one of the most favorable configurations ($\sim 11 \text{ k}_B\text{T}$ per dimer for MTs with 13 or 14 PFs [33–35]). Together with the consistency of our calculated elastic moduli with the observed softening of GMPCPP-MTs or Taxol-stabilized MTs *vs.* GDP-MTs, this strongly suggests that almost the entire energy available from GTP hydrolysis is stored in the form of longitudinal elastic strain.

Lateral coupling and GTP hydrolysis reduce conformational freedom of tubulin in PFs

Pure GMPCPP-MTs and GDP-MTs differ in dimer spacing but are homogeneous in their structure and dynamics, because they consist of mechanochemically equal dimers that explore roughly the same conformational space. However, a key unanswered question is how the MT lattice would accommodate laterally coupled dimers in conflicting conformational states (expanded *vs.* compacted), a situation that is very likely to arise downstream from the growing MT tip. It was previously speculated that such a structural conflict would either weaken the lateral interactions between incompatible dimers or increase the rate of GTPase activity [36,37]. In the latter case, the hydrolysis-triggered compaction of an expanded dimer located next to a compacted dimer would be more favorable. However, testing these hypotheses experimentally is currently challenging.

To get insight into how the presence and conformation of a lateral neighbor affects the compaction dynamics of tubulin in PFs, we constructed atomistic models of double-PF systems in both nucleotide states (Fig. 3*a*; see Methods for model refinement and simulation protocol). We then computed free energy surfaces of the double-PF systems as a function of PF conformations and nucleotide state using the umbrella sampling approach with $\sim 80 \mu\text{s}$ of cumulative simulation time (Fig. 3*b,c*; see Supplementary Fig. 1 for statistical uncertainties). Like the isolated PFs (Fig. 2*b*), the double-PF systems adopted, on average, slightly more expanded conformations relative to its starting cryo-EM structures due to thermal expansion. Also, the constant shift between the two distributions by $0.19 \pm 0.05 \text{ nm}$ was preserved, which was close to the experimentally observed difference of ~ 0.2

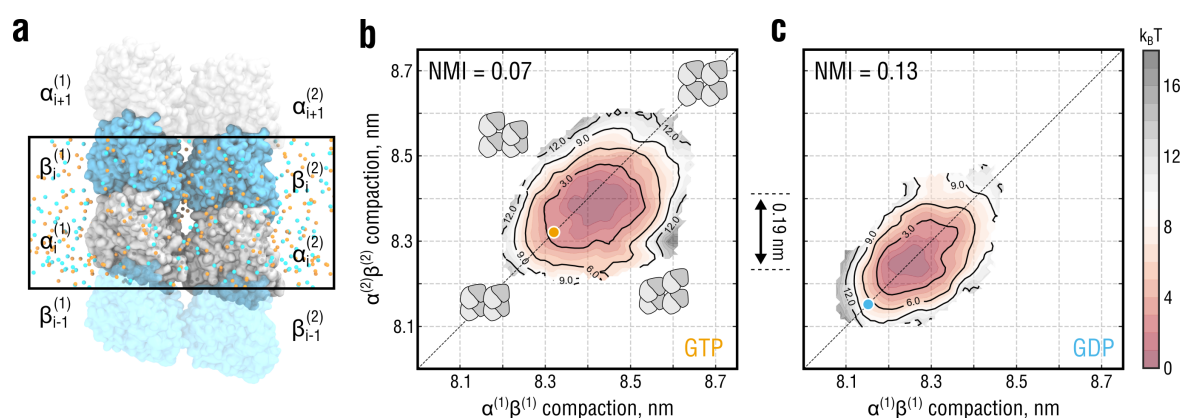


Figure 3. Lateral coupling and nucleotide state affect PF dynamics. **a**, Simulation setup for the double-PF system mimicking a standard (homotypic) lateral interface. Color coding as in Fig. 2a. Water molecules are hidden for clarity. Periodic box is marked by a black rectangle. Individual PFs are labeled as (1) and (2). **b** and **c**, Free energy surfaces of the system in **a** as a function of PF conformations and nucleotide state obtained by umbrella sampling. The surfaces are color-coded by free energy values with an increment of 1 $k_B T$ (dark red to gray). Black solid lines additionally show isoenergetic contours. Orange and cyan circles indicate PF compaction values observed in the cryo-EM densities of GMPCPP- and GDP-MTs, respectively. Cartooned dimers in **b** schematically show the extreme conformations of the double-PF system in which both are similarly expanded or compacted (along the diagonal) or in conflicting conformations (along the anti-diagonal).

nm and, within statistical error, consistent with the difference of 0.25 ± 0.07 nm calculated for the isolated PFs (Fig. 2b).

As described above, we expect each PF in the double-PF system to behave differently depending on the conformational state of the neighbor. In particular, due to the lateral coupling, their motion should be statistically correlated. To quantify this correlation, we used the *normalized mutual information* (NMI) between the dimer spacing fluctuations of each of the two PFs (see Methods for the rigorous definition). For the particular system in Fig. 3a, NMI would be zero if the PFs moved fully independently, and unity if their motion was fully synchronized. Furthermore, a stronger correlation (higher NMI) implies a higher free energy of the double-PF system due to the associated loss of entropy. Vice versa, the joint conformational space increases when the motion of the PFs becomes less correlated, hence lowering the free energy of the double-PF system.

As visible from the free energy surfaces having elliptic shapes extended along the diagonal (Fig. 3b,c) and supported by the calculated NMI values, the conformations of the double-PF system in which the PFs were similarly expanded or compacted were lower in free energy than those in which the PFs adopted conflicting conformations. Thus, the PFs have a mutually restrictive influence on each other, penalizing configurations in which the PF conformations are too different. As a result, the double-PF system exhibits more confined dynamics than would be the case if the PFs were isolated. Furthermore, the confining effect was stronger for the system in GDP-state (a factor of two reduction in NMI relative to GTP-state). Together with the PF stiffening upon GTP hydrolysis (Fig. 2), this suggests that lateral coupling further reduces the conformational space available to tubulin dimers in the double-PF system, making it thermodynamically less favorable than that in GTP-state.

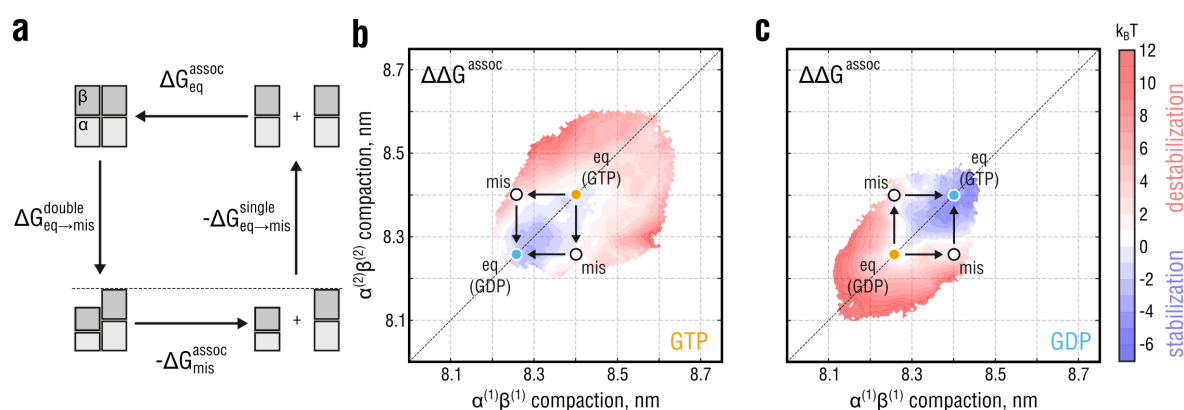


Figure 4. Relative thermodynamic stability of the lateral bond in the double-PF system. **a**, Thermodynamic cycle demonstrating the idea behind estimating the effect of unequal PF conformations on the association free energy between the PFs. While simulating the horizontal transitions (PF association) is computationally more expensive, the free energy changes linked to the vertical transitions (PF compaction) have already been obtained (Fig. 2 and Fig. 3). **b** and **c**, Distributions of the relative stability of the double-PF systems with respect to their equilibrium conformations marked with orange and cyan circles for GTP- and GDP-state, respectively, as a function of PF conformations and nucleotide state. White circles denote conformations with a PF compaction mismatch. Free energy color coding is adjusted such that red (blue) areas correspond to conformations of the double-PF system in which the lateral bond is destabilized (stabilized) relative to equilibrium. White areas correspond to no change in the lateral bond stability.

Nearest-neighbor interactions between PFs modulate GTPase response of tubulin

Our observation that the double-PF system favors conformations in which the PFs are similarly expanded/compacted suggests that the system is less stable when there is a conformational mismatch between the PFs, likely because the lateral bond would be under excessive shear tension. To quantify the extent of lateral bond destabilization by the conformational mismatch between the PFs, we considered a thermodynamic cycle shown in Fig. 4a, following a previous scheme [38]. We assume that the equilibrium conformation of the double-PF system can be changed into the one with a conformational mismatch between the PFs (vertical transitions in Fig. 4a). The free energy cost associated with this transformations ($\Delta G_{eq \rightarrow mis}$) was calculated using our previous umbrella sampling results for both single- and double-PF system (Fig. 2b and Fig. 3b,c; see Supplementary Material). Because the sum over all transition paths in the cycle must vanish, the difference between these values, $\Delta G_{eq \rightarrow mis}^{double} - \Delta G_{eq \rightarrow mis}^{single}$, equals the bond stability of the mismatched double-PF system relative to the equilibrium case, $\Delta \Delta G^{assoc} = \Delta G_{mis}^{assoc} - \Delta G_{eq}^{assoc}$ (horizontal transitions in Fig. 4a). Hence, a positive $\Delta \Delta G^{assoc}$ equally implies that (a) the PF association is less favorable when the PFs are in conflicting compaction states, or that (b) the GTPase response of an expanded dimer is stimulated if its nearest neighbor is in the compacted state. Therefore, from this thermodynamic standpoint, the lateral bond stability is directly linked to the probability of the double-PF system adopting a particular conformation.

Figure 4b,c shows $\Delta \Delta G^{assoc}$ relative to the lowest-energy system configuration (free energy minima in Fig. 3b,c, respectively) as a function of PF conformations and nucleotide state. The calculations suggest that a conformational mismatch between the PFs would have a statistically significant effect on the thermodynamic stability of the double-PF system, corresponding to a change of $\Delta \Delta G^{assoc} = +4.0 \pm 1.6 \text{ k}_B\text{T}$ (equilibrium constant fold-change by ~ 55). In contrast, simultaneous compaction/expansion of the two PFs has no statistically significant effect on the

stability of the double-PF system with a relative change of $\Delta\Delta G^{\text{assoc}} = -1.0 \pm 1.5 \text{ k}_B\text{T}$ (equilibrium constant fold-change by ~ 0.37), implying that the lateral bond is stabilized once the conformational mismatch is resolved. Our results, therefore, directly support the previous ideas that a structural conflict at the lateral interface would weaken it or locally increase the rate of GTPase activity [36,37]. However, not only do we propose that both ideas would be equivalent, but we also estimate the magnitude of lateral bond destabilization and predict that it would be a transient and reversible effect.

Nearest-neighbor interactions between PFs cause long-range correlations in the lattice

The finding that lateral coupling leads to more confined and correlated dynamics of tubulin in the double-PF system is explained by the nearest-neighbor interaction that prevents dimers in the adjacent PFs from adopting conflicting conformations by energetically penalizing local mismatches. It is therefore clear that also the motions of dimers situated in distant PFs should be correlated as a consequence of the elementary short-range interactions shown in Fig. 3*b,c*. However, it is unclear to what extent the nucleotide state would affect such *long-range correlations*. To quantify their magnitude and the dependence on the bound nucleotide in similar minimalist but computationally feasible settings, we constructed a larger PF system comprising 3×1 dimers per periodic length L_z (Fig. 5*a,b*), which allowed us to quantify the statistical correlation between a pair of non-adjacent PFs. From the equilibrium dynamics of this three-PF system, similarly as above, we estimated its free energy landscape as a function of PF conformations and nucleotide state and subsequently disentangled nearest-neighbor interactions and long-range correlations.

As it was unfeasible to perform sufficiently accurate free energy calculations for such a large system, we instead resorted to a Bayesian inference approach that integrates prior knowledge about the energetics of the smaller subsystems (Fig. 2*a* and Fig. 3*a*) to infer the joint free energy distribution of the three-PF system from unbiased MD simulations (see Supplementary Material). To this end, six independent, 600-ns long equilibrium simulations of the three-PF system in each nucleotide state were performed, yielding a total of $\sim 7.2 \mu\text{s}$ of sampling time. The inferred three-dimensional (3D) joint free energy distributions were then pairwise projected onto planes corresponding to two-dimensional (2D) free energy landscapes of adjacent and non-adjacent double-PF subsystems (Fig. 5*c,d*). Consistent with the single-PF and double-PF systems analyzed above (Fig. 2 and Fig. 3), the conformation of the three-PF system in our simulations was more expanded than the underlying cryo-EM structures, while the nucleotide-dependent difference in lattice compaction, again, was preserved.

The NMI values for the non-adjacent free energy landscapes were calculated (NMI_{13}) and compared with those for the adjacent landscapes in the same system (NMI_{12} and NMI_{23}). If the non-adjacent PFs did not interfere, NMI_{13} would be negligible relative to both NMI_{12} and NMI_{23} , yielding almost circular free energy landscapes in Fig. 5*c,d* (center). However, we found that NMI_{13} is only by a factor ~ 0.5 and ~ 0.85 smaller than the values for the directly interacting PFs in GTP- and GDP-state, respectively. This suggests that the correlations between non-adjacent PF induced by the nearest-neighbor PF interactions are enhanced upon GTP hydrolysis.

In fact, several recent findings provide intriguing evidence that weaker intra-lattice correlations might stabilize the MT. First, some MT-stabilizing drugs such as Taxol have been recently shown to increase the lattice heterogeneity of GDP-MTs as compared to drug-free GDP-MTs [39], which resonates with the ability of Taxol to restore the bending flexibility of GDP-MTs [26,40]. Second, a very similar effect on MT stability and mechanical resilience has been reported for acetylated *vs.* wild-type MTs [41,42], likely due to a small but additive allosteric effect of α -tubulin acetylation at residue K40 [43]. In light of our drug- and acetylation-free simulation results, we propose that GTP hydrolysis reduces tubulin axial flexibility and enhances short- and long-range correlations between PFs, thereby leading to a loss of conformational entropy by the MT lattice.

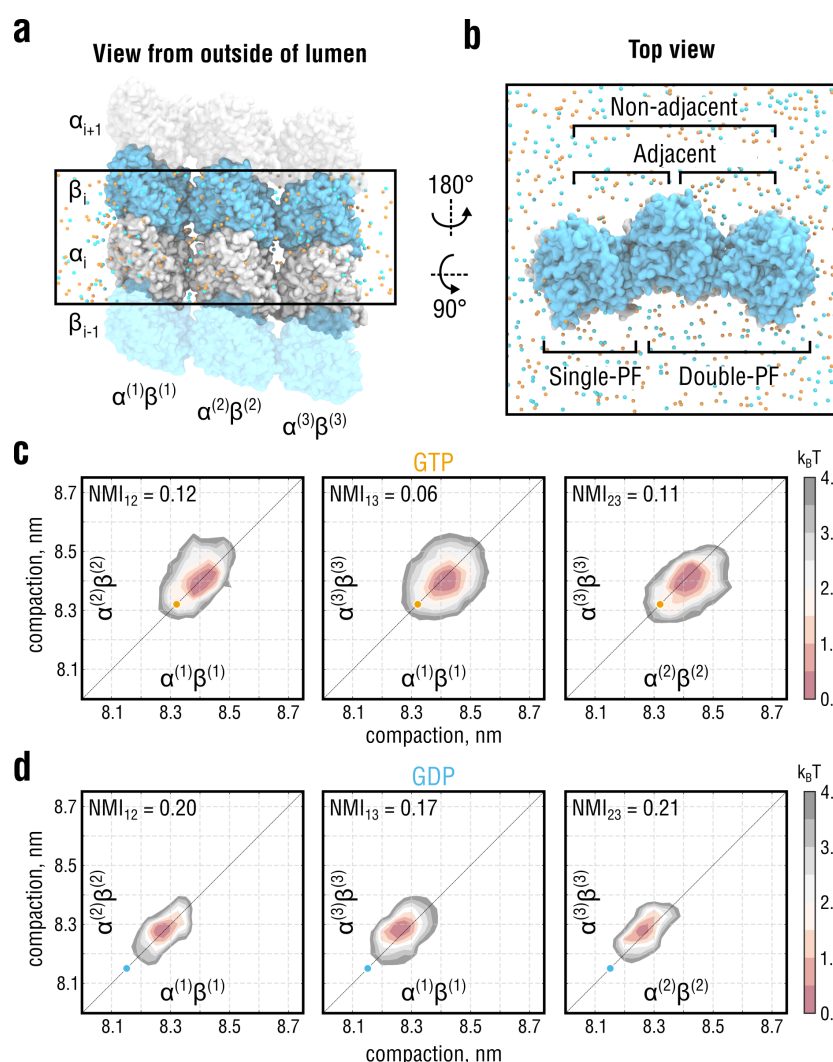


Figure 5. Lateral coupling induces long-range correlations between distant PFs. **a** and **b**, Side and top views of the simulation setup for the three-PF system mimicking a larger segment of the MT lattice. Color coding as in Fig. 2a and Fig. 3a. Water molecules are hidden for clarity. Individual PFs are labeled as (1), (2) and (3). **c** and **d**, Free energy energy landscapes of the system in **a** as a function of PF conformations and nucleotide state. The 3D landscapes were pairwise projected onto planes corresponding to 2D free energy landscapes of adjacent ($\alpha^{(1)}\beta^{(1)} - \alpha^{(2)}\beta^{(2)}$ and $\alpha^{(2)}\beta^{(2)} - \alpha^{(3)}\beta^{(3)}$, left and right, respectively) and non-adjacent PFs ($\alpha^{(1)}\beta^{(1)} - \alpha^{(3)}\beta^{(3)}$, center). Orange and cyan circles indicate PF compaction values observed in the cryo-EM densities of GMPCPP- and GDP-MTs, respectively.

Discussion

Tubulin dimers locked in the MT lattice operate as 'loadable springs' whose 'load' critically depends on both nucleotide state and lattice surrounding. The result is a metastable behavior of MTs because they have to reconcile the favorable dimer-to-lattice binding and the internal strain build-up that is fueled by GTP hydrolysis and has a destabilizing effect. Not surprisingly, it is hard to reach a consensus on precisely where this chemical energy is converted to mechanical strain and spread over the lattice because the system complexity allows various interpretations.

To clarify this issue, we have aimed at a quantitative understanding of the interplay between tubulin intrinsic strain and lateral binding inside straight MT-like compartments. Our results support the following conclusions: (i) there is a two-fold increase in longitudinal lattice tension upon nucleotide hydrolysis, which we attribute to the increased stiffness of GDP-PFs; (ii) lateral coupling between PFs reduces the conformational flexibility of tubulin by entropically penalizing PF conformations that are too different; (iii) restrictive interactions between neighboring PFs induce long-range correlated motions of non-adjacent PFs; (iv) both short- and long-range cooperativity of PF motions is stronger for GDP-PFs suggesting a loss of conformational entropy by MT lattices upon GTP hydrolysis.

By construction, our lattice simulations focus on straight 'infinite' PF systems spanning only one dimer layer per periodic box length, with dimers always interacting with themselves along the MT axis. While such setups are common in the MD field [29, 44–46], they might systematically impact the simulation results by introducing additional correlations along the main axis of symmetry. In the particular case of our simulations, dimers situated in the 'infinite' PFs might be subjected to more longitudinal restraints than would be the case in a long finite MT. However, the size effects are unlikely to significantly affect the conclusions made for two reasons. First, our PF elasticity calculations provide estimates that are largely consistent with previous experimental knowledge, indicating that PF mechanics does not significantly depend on the choice of simulation protocol. Second, we focus primarily on the effect of nucleotide state and always compare simulations of GTP- and GDP-bound systems. Thus, the potential bias introduced by the longitudinal periodic boundaries is further reduced.

Taken together, a model emerges in which the MT lattice stability is not exclusively determined by the nucleotide-dependent dynamics of individual dimers, but more generally, by their non-additive collective behavior. In this work, we provide a thermodynamic explanation for the intrinsic destabilization (farther away from the dynamic tip) which precedes MT breakdown and which relies on the idea that MT lattices gradually accumulate mechanical strain and lose entropy as GTP hydrolysis proceeds. In other words, the MT becomes thermodynamically less and less stable already during the growing phase, which predisposes it to explosive strain release. Exascale atomistic simulations ($\gg 10^6$ atoms) and/or coarse-grained kinetic models can now be used to extrapolate how the results of our study will apply to the time evolution of the MT plus-end tip at much larger spatiotemporal scales.

Methods

Force-field parameters and protonation states

The CHARMM22* force field [47] and the CHARMM-modified TIP3P water model [48] were used in all simulations. GTP/GDP parameters were adapted from those for ATP/ADP implemented in the CHARMM22/CMAP force field [48, 49]. Titration curves of histidines were calculated using the GMCT package [50] and assigned as described previously [17].

Simulation system preparation and cryo-EM refinement

Initial models for the tubulin dimers were obtained from PDB IDs 3JAT (GMPCPP) and 3JAS (GDP) [21] by extracting the central dimer from the 3×2 lattice patches (chains A and H in the original PDBs). GMPCPP was converted into GTP by replacing the carbon atom between α - and β -phosphate with an oxygen atom. The missing loop in the α -subunit (residues 38–46) was modelled in for structure consistency using MODELLER version 9.17 [51] but excluded from further refinement. Unlike in our previous study [17], we did not include the missing C-termini (α :437–451 and β :426–445) in our simulations to reduce the system size and reach the best possible sampling. Unless differently specified, all structure and map manipulations were performed using UCSF Chimera [52] or VMD [53].

In all refinement simulations, the following data sets were used: EMD-6352 and EMD-6353 for symmetrized cryo-EM reconstructions of 14-PF GMPCPP- and GDP-MTs decorated with kinesin [21]. To create 'infinite' single-, double-, and three-PF systems, where the actual simulated part comprises exactly one layer of dimers and is coupled to copies of itself through axial periodic boundaries, we first constructed finite PF systems comprising two layers of dimers in the axial direction. To this end, subsections of the cryo-EM maps with the desired PF topology were extracted using an orthorhombic box, and the single dimer models were rigid-body fitted into the PF maps. The constructed PF systems were solvated in a triclinic water box of size $8.0 \times 8.0 \times 22.0 \text{ nm}^3$ (single-PF), $12.7 \times 12.7 \times 22.0 \text{ nm}^3$ (double-PF), or $19.0 \times 19.0 \times 22.0 \text{ nm}^3$ (three-PF). The systems were then neutralized with 150 mM KCl.

Refinement was done with correlation-driven molecular dynamics implemented as a custom module in the GROMACS 5.0.7 package [54], following our previously published protocols [28]. Briefly, we used the cold-fitting protocol with the longest refinement time (*i.e.* $T = 100 \text{ K}$ and total run time of 50 ns) followed by 15 ns of simulated annealing. The starting values for the biasing strength and the simulated map resolution were set to $1 \times 10^5 \text{ kJ mol}^{-1}$ and 0.6 nm and linearly ramped to $5 \times 10^5 \text{ kJ mol}^{-1}$ and 0.2 nm, respectively. The quality of the resulting models and the goodness of fit were ensured by calculating common stereochemical and correlation metrics (Supplementary Table 1).

MD simulations

The finite PF models were converted into 'infinite' PF models by removing the extra tubulin monomers and nucleotides. Water and ion atoms were then trimmed to conform to the experimental value of the axial periodic parameter L_z , namely, 8.31 nm for GMPCPP-MTs and 8.15 nm for GDP-MTs [21]. The number of ions in the trimmed water shell was fixed such as to keep the systems neutral and to maintain the ionic strength of 150 mM KCl. All subsequent MD simulations were carried out with GROMACS 5.0.7 [54]. Lennard-Jones and short-range electrostatic interactions were calculated with a 0.95-nm cutoff, while long-range electrostatic interactions were treated using particle-mesh Ewald summation [55] with a 0.12-nm grid spacing. The bond lengths were constrained using the LINCS algorithm [56] (hydrogen bonds during equilibration and all bonds in the production runs). Velocity rescaling [57] with a heat bath coupling constant of 0.5 ps was used to control the temperature for solute and solvent separately. Applying virtual site constraints [58] allowed us to increase the integration step size to 4 fs in the production runs. Center-of-mass correction was applied to solute and solvent separately every 100 steps.

With the above parameters fixed, the equilibration protocol consisted of the following steps: (i) energy minimization using steepest descent; (ii) short NVT equilibration for 1 ns at $T = 100 \text{ K}$ with position restraints on heavy atoms and using a 1-fs integration time step; (iii) gradually heating up the system to 300 K within 10 ns in the NPT ensemble (Berendsen barostat [59] with a 5-ps coupling constant) using a 2-fs integration time step; (iv) equilibration in the NPT ensemble for 30 ns using isotropic Parrinello-Rahman barostat [60] with a 5-ps coupling constant and using a 2-fs integration time step; (v) equilibration in the NPT ensemble for 100 ns using semi-isotropic Parrinello-Rahman barostat with a 5-ps coupling constant and using a 2-fs time step. The last frame of step (v) was used to spawn stress-free production runs, stress-strain calculations, and umbrella sampling simulations.

Derivation of the compaction reaction coordinate

We carried out 20 independent, 1- μs long equilibrium simulations of the single-PF system in GTP-state, where the starting structure for each simulation was drawn every 150 ns from a 'seeding' simulation trajectory of 3 μs . For the single-PF system in GDP-state, we carried out 10 independent simulations (1 μs each) with the starting configurations drawn every 300 ns from a 3- μs 'seeding' trajectory. We then extracted backbone atoms (N , C_α , C and O) and excluded flexible protein regions (α : 38-46, α : 278-284 and β : 276-284) from further analysis.

Partial least-squares (PLS) functional mode analysis [61,62] was then applied to the combined simulation set (both GTP- and GDP-state) to derive the collective mode of motion that correlated best with the fluctuations of the axial periodic dimension L_z and had the largest variance in terms of molecular motion. The linear regression model was trained on the first half of the GTP data set ($\sim 13 \mu s$) and the second half of the GDP data set ($\sim 7 \mu s$), and the remaining halves were used for cross-validation. The cross-validation revealed that the ensemble-weighted collective mode (corresponds to the solution with one PLS component by construction) had correlation coefficients of 0.9 (training set) and 0.85 (validation set), hence yielding a robust representation of the conformational transition between the expanded GTP- and compacted GDP-state (Fig. 2*b*). A visualization of this transition is shown in Supplementary Movie 1.

Normalized mutual information

In theory, the mutual information (MI) between two stochastic quantities χ_1 and χ_2 is

$$I(\chi_1, \chi_2) = H(\chi_1) + H(\chi_2) - H(\chi_1, \chi_2), \quad (1)$$

where $H(\chi_i) = -\int p_i(\chi_i) \log p_i(\chi_i) d\chi_i$ is the entropy and $p_i(\chi_i)$ is the probability density of χ_i ($i = 1, 2$). The joint entropy $H(\chi_1, \chi_2)$ is defined similarly and requires knowledge of the joint probability density $p_{12}(\chi_1, \chi_2)$.

In practice, calculation of the MI is very sensitive to how the underlying probability densities are discretized. Too coarse-grained discretization leads to an underestimation and too detailed discretization leads to an overestimation of the MI. We therefore used the Jack Knifed estimate that is known to be a low bias estimate of the MI and robust to discretization bin size [63]. It is defined by substituting the entropy in Eq. 1 with the following estimate $\hat{H}_{JK}(\chi_i) = N\hat{H}(\chi_i) - \frac{N-1}{N} \sum_{j=1}^N \hat{H}_{-j}(\chi_i)$, where $\hat{H}(\chi_i)$ is the entropy calculated by a straightforward discretization and $\hat{H}_{-j}(\chi_i)$ is the same as $\hat{H}(\chi_i)$ but when leaving out bin value j , and N is the total number of bins. The normalized mutual information is then defined as:

$$\text{NMI}_{12} = \frac{\hat{I}_{JK}(\chi_1, \chi_2)}{\sqrt{\hat{H}_{JK}(\chi_1) \hat{H}_{JK}(\chi_2)}}. \quad (2)$$

Estimating MT bending stiffness from previous experimental data

The experimental values for MT bending stiffnesses and the respective uncertainties shown in Fig. 2*d* were calculated using inverse-variance weighting [64]. Given a set of independent measurements y_i with variances σ_i^2 , the consensus inverse-variance mean and standard deviation are given by $\hat{y} = \sum_i w_i y_i / \sum_i w_i$ and $\hat{\sigma} = \sqrt{1 / \sum_i w_i}$, where the weights $w_i = 1/\sigma_i^2$. For GDP-MTs and GDP-MTs stabilized with Taxol, we used the $E \times I$ values estimated by quantifying thermal fluctuations of MTs, as summarized in [26] and [27]. As there were only few measurements of GMPCPP-MTs in the cited publications, we extended the set by considering further thermal fluctuation studies [40, 65, 66].

Code and supplementary data

All refined starting structures are provided as Supplementary Data Sets. Complete MD trajectories that support the findings are available from the corresponding authors upon request. Unless explicitly specified, all numerical calculations were carried out using Python 2.7 [67] and Cython [68]. Supplementary Material further includes all supplementary figures and tables as well as detailed information on stress-strain calculations, estimation of the per-dimer elastic strain energy, umbrella sampling simulations, estimation of the relative lateral bond stability, and Bayesian inference of the joint free energy distribution for the three-PF system.

Acknowledgments

We thank Rui Zhang (Washington University in St. Louis, USA) and Eva Nogales (UC Berkeley, USA) for insightful discussions and for kindly providing the microtubule cryo-EM reconstructions; Gregory Bubnis (UC San Francisco, USA) and Thomas Ullmann (MPI-BPC, Göttingen, Germany) for suggestions about free energy calculations and error estimation. The work was supported by the Max Planck Society and the German Research Foundation via the grant IG 109/1-1. Computational resources were provided by the North-German Supercomputing Alliance (Berlin/Göttingen, Germany) as well as by the Max Planck Computing and Data Facility and the Leibniz Supercomputing Centre (Garching, Germany).

References

1. H. Sosa and R. A. Milligan. Three-dimensional Structure of ncd-decorated Microtubules Obtained by a Back-projection Method. *J. Mol. Biol.*, 260(5):743–755, 1996.
2. E. Nogales, M. Whittaker, R. A. Milligan, and K. H. Downing. High-Resolution Model of the Microtubule. *Cell*, 96(1):79–88, 1999.
3. E. Nogales, S. G. Wolf, and K. H. Downing. Structure of the alpha beta tubulin dimer by electron crystallography. *Nature*, 391(6663):199–203, 1998.
4. M. F. Carlier, D. Didry, and D. Pantaloni. Microtubule Elongation and Guanosine 5'-Triphosphate Hydrolysis. Role of Guanine Nucleotides in Microtubule Dynamics. *Biochemistry*, 26(14):4428–4437, 1987.
5. T. Mitchison and M. Kirschner. Dynamic instability of microtubule growth. *Nature*, 312(5991):237–42, 1984.
6. M. Dogterom and B. Yurke. Measurement of the force-velocity relation for growing microtubules. *Science (80-.)*, 278(5339):856–60, 1997.
7. E. L. Grishchuk, M. I. Molodtsov, F. I. Ataullakhanov, and J. R. McIntosh. Force production by disassembling microtubules. *Nature*, 438(7066):384–388, 2005.
8. J. W. Driver, E. A. Geyer, M. E. Bailey, L. M. Rice, and C. L. Asbury. Direct measurement of conformational strain energy in protofilaments curling outward from disassembling microtubule tips. *Elife*, 6:e28433, 2017.
9. J. R. Simon and E. D. Salmon. The structure of microtubule ends during the elongation and shortening phases of dynamic instability examined by negative-stain electron microscopy. *J. Cell Sci.*, 96 (Pt 4):571–82, aug 1990.
10. E. M. Mandelkow, E. Mandelkow, and R. A. Milligan. Microtubule dynamics and microtubule caps: a time-resolved cryo- electron microscopy study. *J. Cell Biol.*, 114(5):977–991, 1991.
11. R. Melki, M. F. Carlier, D. Pantaloni, and S. N. Timasheff. Cold depolymerization of microtubules to double rings: geometric stabilization of assemblies. *Biochemistry*, 28(23):9143–9152, 1989.
12. D. Chrétien, S. D. Fuller, and E. Karsenti. Structure of growing microtubule ends: Two-dimensional sheets close into tubes at variable rates. *J. Cell Biol.*, 129(5):1311–1328, 1995.
13. T. Müller-Reichert, D. Chretien, F. Severin, and A. A. Hyman. Structural changes at microtubule ends accompanying GTP hydrolysis: Information from a slowly hydrolyzable analogue of GTP, guanylyl (α,β)methylenediphosphonate. *Proc. Natl. Acad. Sci.*, 95(7):3661–3666, 1998.

14. J. Atherton, M. Stouffer, F. Francis, and C. A. Moores. Microtubule architecture in vitro and in cells revealed by cryo-electron tomography. *Acta Crystallogr. Sect. D Struct. Biol.*, 74(6):572–584, 2018.
15. J. R. McIntosh, E. O’Toole, G. Morgan, J. Austin, E. Ulyanov, F. Ataullakhanov, and N. Gudimchuk. Microtubules grow by the addition of bent guanosine triphosphate tubulin to the tips of curved protofilaments. *J. Cell Biol.*, 217(8):2691–2708, 2018.
16. H. W. Wang and E. Nogales. Nucleotide-dependent bending flexibility of tubulin regulates microtubule assembly. *Nature*, 435(7044):911–915, 2005.
17. M. Igaev and H. Grubmüller. Microtubule assembly governed by tubulin allosteric gain in flexibility and lattice induced fit. *Elife*, 7:e34353, 2018.
18. V. A. Fedorov, P. S. Orekhov, E. G. Kholina, A. A. Zhmurov, F. I. Ataullakhanov, I. B. Kovalenko, and N. B. Gudimchuk. Mechanical properties of tubulin intra- and inter-dimer interfaces and their implications for microtubule dynamic instability. *PLOS Comput. Biol.*, 15(8):e1007327, 2019.
19. A. A. Hyman, D. Chrétien, I. Arnal, and R. H. Wade. Structural changes accompanying GTP hydrolysis in microtubules: information from a slowly hydrolyzable analogue guanylyl-(alpha,beta)-methylene-diphosphonate. *J. Cell Biol.*, 128(1-2):117–25, 1995.
20. G. M. Alushin, G.C. Lander, E. H. Kellogg, R. Zhang, D. Baker, and E. Nogales. High-Resolution Microtubule Structures Reveal the Structural Transitions in $\alpha\beta$ -Tubulin upon GTP Hydrolysis. *Cell*, 157(5):1117–1129, 2014.
21. R. Zhang, G. M. Alushin, A. Brown, and E. Nogales. Mechanistic origin of microtubule dynamic instability and its modulation by EB proteins. *Cell*, 162(4):849–859, 2015.
22. R. Zhang, B. LaFrance, and E. Nogales. Separating the effects of nucleotide and EB binding on microtubule structure. *Proc. Natl. Acad. Sci.*, 115(27):E6191–E6200, 2018.
23. S. W. Manka and C. A. Moores. The role of tubulin-tubulin lattice contacts in the mechanism of microtubule dynamic instability. *Nat. Struct. Mol. Biol.*, 25(7):607–615, 2018.
24. S. W. Manka and C. A. Moores. Microtubule structure by cryo-EM: snapshots of dynamic instability. *Essays Biochem.*, 62(6):737–751, 2018.
25. B. J. Harris, J. L. Ross, and T. L. Hawkins. Microtubule seams are not mechanically weak defects. *Phys. Rev. E*, 97(6):1–7, 2018.
26. T. Hawkins, M. Mirigian, M. Selcuk Yasar, and J. L. Ross. Mechanics of microtubules. *J. Biomech.*, 43(1):23–30, 2010.
27. E. Memet, F. Hilitski, M. A. Morris, W. J. Schwenger, Z. Dogic, and L. Mahadevan. Microtubules soften due to cross-sectional flattening. *Elife*, 7:e34695, 2018.
28. M. Igaev, C. Kutzner, L. V. Bock, A. C. Vaiana, and H. Grubmüller. Automated cryo-EM structure refinement using correlation-driven molecular dynamics. *Elife*, 8:e43542, 2019.
29. D. B. Wells and A. Aksimentiev. Mechanical properties of a complete microtubule revealed through molecular dynamics simulation. *Biophys. J.*, 99(2):629–637, 2010.
30. M. Kikumoto, M. Kurachi, V. Tosa, and H. Tashiro. Flexural rigidity of individual microtubules measured by a buckling force with optical traps. *Biophys. J.*, 90(5):1687–1696, 2006.

31. S. Ray, E. Meyhöfer, R. A. Milligan, and J. Howard. Kinesin follows the microtubule's protofilament axis. *J. Cell Biol.*, 121(5):1083–1093, 1993.
32. M. Caplow, R. L. Ruhlén, and J. Shanks. The free energy for hydrolysis of a microtubule-bound nucleotide triphosphate is near zero: All of the free energy for hydrolysis is stored in the microtubule lattice. *J. Cell Biol.*, 127(3):779–788, 1994.
33. D. Chrétien, F. Metoz, F. Verde, E. Karsenti, and R. H. Wade. Lattice defects in microtubules: protofilament numbers vary within individual microtubules. *J. Cell Biol.*, 117(5):1031–40, 1992.
34. D. Chrétien and S.D. Fuller. Microtubules switch occasionally into unfavorable configurations during elongation. *J. Mol. Biol.*, 298(4):663–676, 2000.
35. V. Hunyadi, D. Chrétien, and I. M. Jánosi. Mechanical stress induced mechanism of microtubule catastrophes. *J. Mol. Biol.*, 348(4):927–938, 2005.
36. G. J. Brouhard and L. M. Rice. Microtubule dynamics: an interplay of biochemistry and mechanics. *Nat. Rev. Mol. Cell Biol.*, 19(7):451–463, 2018.
37. T. Kim and L. M. Rice. Long-range, through-lattice coupling improves predictions of microtubule catastrophe. *Mol. Biol. Cell*, 30(12):1451–1462, 2019.
38. A. W. Yee, M. Aldeghi, M. P. Blakeley, A. Ostermann, P. J. Mas, M. Moulin, D. de Sanctis, M. W. Bowler, C. Mueller-Dieckmann, E. P. Mitchell, M. Haertlein, B. L. de Groot, E. Boeri Erba, and V. T. Forsyth. A molecular mechanism for transthyretin amyloidogenesis. *Nat. Commun.*, 10(1):925, 2019.
39. E. H. Kellogg, N. M.A. Hejab, S. Howes, P. Northcote, J. H. Miller, J. F. Díaz, K. H. Downing, and E. Nogales. Insights into the Distinct Mechanisms of Action of Taxane and Non-Taxane Microtubule Stabilizers from Cryo-EM Structures. *J. Mol. Biol.*, 429(5):633–646, mar 2017.
40. B. Mickey and J. Howard. Rigidity of microtubules is increased by stabilizing agents. *J. Cell Biol.*, 130(4):909–917, 1995.
41. D. Portran, L. Schaedel, Z. Xu, M. Théry, and M. V. Nachury. Tubulin acetylation protects long-lived microtubules against mechanical ageing. *Nat. Cell Biol.*, 19(4):391–398, 2017.
42. Z. Xu, L. Schaedel, D. Portran, A. Aguilar, J. Gaillard, M. P. Marinkovich, M. Théry, and M. V. Nachury. Microtubules acquire resistance from mechanical breakage through intraluminal acetylation. *Science (80-.)*, 356(6335):328–332, 2017.
43. L. Eshun-Wilson, R. Zhang, D. Portran, M. V. Nachury, D. B. Toso, T. Löhr, M. Vendruscolo, M. Bonomi, J. S. Fraser, and E. Nogales. Effects of α -tubulin acetylation on microtubule structure and stability. *Proc. Natl. Acad. Sci.*, 116(21):10366–10371, may 2019.
44. J.-W. Chu and G. A. Voth. Allostery of actin filaments: Molecular dynamics simulations and coarse-grained analysis. *Proc. Natl. Acad. Sci.*, 102(37):13111–13116, 2005.
45. B. Luan and A. Aksimentiev. Strain Softening in Stretched DNA. *Phys. Rev. Lett.*, 101(11):118101, sep 2008.
46. D. Bochicchio, S. Kwangmettatam, T. Kudernac, and G. M. Pavan. How Defects Control the Out-of-Equilibrium Dissipative Evolution of a Supramolecular Tubule. *ACS Nano*, 13(4):4322–4334, 2019.
47. S. Piana, K. Lindorff-Larsen, and D. E. Shaw. How robust are protein folding simulations with respect to force field parameterization? *Biophys. J.*, 100(9):L47–L49, 2011.

48. A. D. MacKerell, D. Bashford, M. Bellott, R. L. Dunbrack, J. D. Evanseck, M. J. Field, S. Fischer, J. Gao, H. Guo, S. Ha, D. Joseph-McCarthy, L. Kuchnir, K. Kuczera, F. T. K. Lau, C. Mattos, S. Michnick, T. Ngo, D. T. Nguyen, B. Prodhom, W. E. Reiher, B. Roux, M. Schlenkrich, J. C. Smith, R. Stote, J. Straub, M. Watanabe, J. Wiórkiewicz-Kuczera, D. Yin, and M. Karplus. All-Atom Empirical Potential for Molecular Modeling and Dynamics Studies of Proteins. *J. Phys. Chem. B*, 102(18):3586–3616, 1998.
49. A. D. Mackerell, M. Feig, and C. L. Brooks. Extending the treatment of backbone energetics in protein force fields: Limitations of gas-phase quantum mechanics in reproducing protein conformational distributions in molecular dynamics simulations. *J. Comput. Chem.*, 25(11):1400–1415, 2004.
50. R. T. Ullmann and G. M. Ullmann. GMCT : A Monte Carlo simulation package for macromolecular receptors. *J. Comput. Chem.*, 33(8):887–900, 2012.
51. A. Fiser, R. K. Do, and A. Sali. Modeling of loops in protein structures. *Protein Sci.*, 9(9):1753–73, 2000.
52. E. F. Pettersen, T. D. Goddard, C. C. Huang, G. S. Couch, D. M. Greenblatt, E. C. Meng, and T. E. Ferrin. UCSF Chimera - A visualization system for exploratory research and analysis. *J. Comput. Chem.*, 25(13):1605–1612, 2004.
53. W. Humphrey, A. Dalke, and K. Schulten. VMD: Visual molecular dynamics. *J. Mol. Graph.*, 14(1):33–38, 1996.
54. M. J. Abraham, T. Murtola, R. Schulz, S. Páll, J. C. Smith, B. Hess, and E. Lindahl. GROMACS: High performance molecular simulations through multi-level parallelism from laptops to supercomputers. *SoftwareX*, 1-2:19–25, 2015.
55. U. Essmann, L. Perera, M. L. Berkowitz, T. Darden, H. Lee, and L. G. Pedersen. A smooth particle mesh Ewald method. *J. Chem. Phys.*, 103(19):8577–8593, 1995.
56. B. Hess, C. Kutzner, D. van der Spoel, and E. Lindahl. GROMACS 4: Algorithms for Highly Efficient, Load-Balanced, and Scalable Molecular Simulation. *J. Chem. Theory Comput.*, 4(3):435–47, 2008.
57. G. Bussi, D. Donadio, and M. Parrinello. Canonical sampling through velocity rescaling. *J. Chem. Phys.*, 126(1):014101, 2007.
58. K. A. Feenstra, B. Hess, and H. J. C. Berendsen. Improving efficiency of large time-scale molecular dynamics simulations of hydrogen-rich systems. *J. Comput. Chem.*, 20(8):786–798, 1999.
59. H. J. C. Berendsen, J. P. M. Postma, W. F. van Gunsteren, A. DiNola, and J. R. Haak. Molecular dynamics with coupling to an external bath. *J. Chem. Phys.*, 81(8):3684–3690, 1984.
60. M. Parrinello and A. Rahman. Polymorphic transitions in single crystals: A new molecular dynamics method. *J. Appl. Phys.*, 52(12):7182–7190, 1981.
61. Jochen S. Hub, Bert L. De Groot, and David van der Spoel. g-wham - a free Weighted Histogram Analysis implementation including robust error and autocorrelation estimates. *J. Chem. Theory Comput.*, 6(12):3713–3720, 2010.
62. T. Krivobokova, R. Briones, J. S. Hub, A. Munk, and B. L. De Groot. Partial least-squares functional mode analysis: Application to the membrane proteins AQP1, Aqy1, and CLC-ec1. *Biophys. J.*, 103(4):786–796, 2012.

63. L. Paninski. Estimation of Entropy and Mutual Information. *Neural Comput.*, 15(6):1191–1253, 2003.
64. J. Hartung, G. Knapp, and B. K. Sinha. *Statistical Meta-Analysis with Applications*. Wiley Series in Probability and Statistics. John Wiley & Sons, Inc., 2008.
65. T. L. Hawkins, D. Sept, B. Mogessie, A. Straube, and J. L. Ross. Mechanical properties of doubly stabilized microtubule filaments. *Biophys. J.*, 104(7):1517–1528, 2013.
66. K. Kawaguchi and A. Yamaguchi. Temperature dependence rigidity of non-taxol stabilized single microtubules. *Biochem. Biophys. Res. Commun.*, 402(1):66–69, 2010.
67. Python Software Foundation. Python Language Reference, version 2.7. February 6, 2017, 2017.
68. S. Behnel, R. Bradshaw, C. Citro, L. Dalcin, D. S. Seljebotn, and K. Smith. Cython: The Best of Both Worlds. *Comput. Sci. Eng.*, 13(2):31–39, 2011.